

1 *Revised version submitted to Mineralogy and Petrology the 21st of June 2011*

2

3 **Timescale of open-reservoir evolution beneath the south Cleft**
4 **segment, Juan de Fuca ridge.**

5

6 **Cordier Carole, Caroff Martial, Rannou Eric**

7

8

9

10

11 C. Cordier (✉) and M. Caroff

12 Université Européenne de Bretagne, Université de Brest; UMR n°6538 “Domaines

13 Océaniques” et IUEM; 6 avenue Le Gorgeu, C.S. 93837,

14 29238 Brest Cedex 3, France.

15 E_mail: cordier@unisi.it

16

17 C. Cordier

18 Present address: Museo Nazionale dell’Antartide, Università di Siena, Via Laterina 8,

19 53100 Siena, Italy.

20

21 E. Rannou

22 Université Européenne de Bretagne, Université de Brest; UMR n°6205 “Laboratoire de

23 Mathématiques”; 6 avenue Le Gorgeu, C.S. 93837,

24 29238 Brest Cedex 3, France.

25 **Abstract** Lavas erupted at the southern end of the intermediate Juan de Fuca ridge (Cleft
26 segment) are mostly cogenetic and their chemical diversity results from melt evolution in an
27 open magma system. In the present study, we apply a theoretical model allowing the time
28 evolution of this periodically recharged and tapped magma chamber to be estimated. In our
29 mathematical procedure, the melt quantity supplied to the reservoir varies through time
30 following a sinusoidal function. The rare earth element concentrations in the refilling melt
31 were calculated on the basis of the REE distribution in lavas. This theoretical composition is
32 akin to that previously estimated for a Mg#70 MORB from mineralogical and chemical data.
33 Then, we approached the temporal evolution of the reservoir using a set of suitable parameters
34 deduced from the geometry of the crust and magma system beneath the Cleft segment.
35 Particularly, we considered two end-members scenarios for the melt repartition through the
36 magma reservoir beneath the Cleft segment: the “gabbro glacier” model (crystal nucleation
37 and growth occur within one single melt lens and crystals subside vertically and laterally) and
38 the “sheeted sill” model (crystallization takes place within a network of connected sills
39 located at various depths in the crust). We estimated that the magma chamber is refilled every
40 thousand years and that the melt resides approximately one hundred years within the
41 reservoir.

42
43 **Keywords:** oceanic crust; mid-ocean ridge basalts; magmatic periodicity; open-system
44 reservoir; replenishment melt; residence time

46 **Introduction**

47
48 To develop quantitative models for magmatic systems beneath fast- and intermediate-
49 spreading ridges, constraints on the timescales of processes such as melting, differentiation,

50 and crystallization are required. Temporal information is still difficult to estimate from
51 geological and geochemical data. For two decades, more and more studies were based on
52 samples collected from holes drilled into the upper oceanic crust (Wilson et al. 2006), from
53 across-ridge profiles (Davis et al. 2008), from crust exposures along slightly tectonized
54 fracture zones or propagating rifts (Karson et al. 2002a; Karson et al. 2002b; Pollock et al.
55 2005; Cordier et al. 2007), and from ophiolite exposures (Pallister and Hopson 1981;
56 Smewing 1981; Einaudi et al. 2003). These studies provided constraints on the relative
57 chronology of the volcanics and then on the time-related chemical variations in lavas erupted
58 from a single ridge segment. Further seismological data have shown that, beneath spreading
59 ridges, the melt lens is a dynamic object. Its volume and depth are tied to the eruption and
60 replenishment cycles of the magma reservoir (Hussenoeder et al. 1996; Hooft et al. 1997;
61 Singh et al. 1998). The vertical movements of the melt lens were also documented by
62 petrological evidences of reheating, hydrous partial melting and assimilation of the base of the
63 sheeted dikes (Gillis and Coogan 2002; Koepke et al. 2008; France et al. 2010). On the whole,
64 these results evidence cyclic variations of the thermal state of the axial magma chamber,
65 related to fluctuations of the balance between magma recharge and hydrothermal cooling
66 beneath spreading ridges.

67 We propose here to characterize the rare earth element (REE) concentrations in melts
68 that evolved in a postulated periodically refilled reservoir and to estimate the REE
69 composition of the replenishment melt, the average crystallization rate, the period of magma
70 recharge and the average magma residence time, using the mathematical procedure developed
71 by Rannou et al. (2006). We will consider the lavas erupted at the southern end of Juan de
72 Fuca ridge axis: those collected at and near the axis (Smith et al. 1994; Stakes et al. 2006) and
73 those collected along the northern wall of the Western Blanco Depression, which truncates the
74 crust accreted at the Juan de Fuca axis since 1.4 Ma (Cordier et al. 2007). In addition to

75 chemical data, the model resolution requires the estimation of some geological parameters
76 (Fig. 1) related to the architecture of the crust and to the geometry of the magma reservoir. A
77 broad approach of these parameters has already been discussed by Rannou et al. (2006). Here,
78 their estimation will be made to consider the specificities of the reservoir beneath fast- and
79 intermediate-spreading ridges. Indeed, it is well-established that beneath these ridges, the
80 axial magma chamber includes one or several thin lens(es) of partially crystallized melt
81 located just below the sheeted dike complex and overlying a partially molten region (Detrick
82 et al. 1987; Sinton and Detrick 1992; Boudier et al. 1996). However, the role of this (these)
83 melt lens(es) in the storage and differentiation of mid-ocean ridge basalts (MORBs) and in the
84 accretion of the lower crust is still debated. The current models are represented by two end-
85 members. According to the “gabbro glacier” model (GG, Fig. 1b), crystal nucleation and
86 growth occur within one single melt lens and crystals subside vertically and laterally to form
87 the lower crust as oceanic crust spreads away from the ridge axis (Henstock et al. 1993;
88 Phipps Morgan and Chen 1993; Quick and Denlinger 1993; Henstock 2002). Conversely, the
89 “sheeted sill” model (SS, Fig. 1c) considers that crystallization takes place *in situ* within a
90 network of connected sills located at various depths in the crust and that the seismically
91 imaged melt lens is simply the shallowest of them (Boudier et al. 1996; Kelemen et al. 1997;
92 Korenaga and Kelemen 1998; Garrido et al. 2001). The relative efficiency of these two
93 scenarios depends on the cooling rate of the lower oceanic crust and thus on the interplay
94 between heat supply through melt recharge and heat extraction through conduction and
95 hydrothermal circulations. In turn, these models have diverging consequences on the
96 repartition of the amount of crystallization with depth and on the expected degree of
97 differentiation of the melt refilling the upper melt lens. For example, if heat removal by
98 hydrothermal circulations is more efficient from the base of the dyke complex than from
99 deeper in the lower crust, the majority of crystallization probably will occur in the upper melt

100 lens rather than *in situ* within the gabbroic section. In this case, primitive melts will be
101 delivered to the upper lens. In our modeling, we thus evaluated the role of *in situ*
102 crystallization and, through the quantity of melt in the magma chamber, the respective
103 contribution of the upper melt lens and of the lower sills during magma differentiation.

104

105 **Open magma system beneath the southern Cleft segment of the Juan de Fuca ridge**

106

107 Recent evolution documented by the geochemistry of the Cleft lavas

108

109 The Juan de Fuca ridge separates the Pacific and Juan de Fuca plates (Fig. 2a, inset).

110 Its southern 60 km-long Cleft segment (45°03'N to 44°27'N) spreads at an intermediate rate

111 (56 mm/y, Wilson 1993) and is bounded by the Vance segment on the north and the Blanco

112 fracture zone on the south (Fig. 2a). The segment axis is characterized by a dome rifted by a

113 large transient graben (Normark et al. 1983). Along the southern part of the segment, the

114 graben floor is notched by a central narrow depression, named cleft or axial summit collapse

115 trough, which results from the collapse of volcanic structures, lava lakes or thick volcanic

116 flows (Chadwick and Embley 1998; Stakes et al. 2006). The roof of discrete melt lenses has

117 been seismically imaged at ~2 km of depth into the crust and over 10 km-long continuous

118 intervals (Canales et al. 2005; Canales et al. 2006). In the southern part of the Cleft segment,

119 the melt lens would be 100-m thick and 900-m wide and partially crystallized, comprising

120 only ~ 30 vol. % of melt (Canales et al. 2006).

121 The Cleft lavas are normal MORBs resulting from the partial melting of a depleted

122 and quite homogeneous mantle source with constant melting extents (Smith et al. 1994;

123 Stakes et al. 2006). The lavas display a large range of compositions ($3.5 < \text{MgO wt. \%} < 8$,

124 Fig. 2b) that are thought to mostly result from the differentiation of primary tholeiitic melts in

125 open-system magma reservoirs (Fig. 2c). The correlation between lava ages, degrees of
126 differentiation, and latitudes (Fig. 2b, Smith et al. 1994) is consistent with the coexistence of
127 several discrete magma chambers along the Cleft segment, as observed in seismic profiles
128 (Canales et al. 2005), and with the increase of the melt lens crystallinity from north to south
129 inferred from geophysical studies (Canales et al. 2006). In the northern part, young and
130 primitive basalts prevail (Fig. 2b) and would originate from a recently recharged magma
131 reservoir. Southward, lavas are more evolved (Fig. 2b) and would derive from a progressively
132 waned chamber, in response of the decrease of the magma supply (Smith et al. 1994). Thus,
133 along the segment, the magma chambers are in different stage of evolution, which can be
134 interpreted as reflecting the cyclic evolution through time of the axial magma reservoirs, as
135 already proposed for the East Pacific Rise by Lagabriele and Cormier (1999) and for the
136 north-south propagating spreading center of the North Fiji Basin by Caroff and Fleutelot
137 (2003).

138 The southernmost magma chamber that we study is interpreted to be in a waning state.
139 Dacitic glass has been collected at the intersection between the southern Cleft segment and
140 the Blanco fracture zone (Fig. 2). The dacitic melt could correspond to a differentiated
141 product erupted from cooler and distal edges of the melt lens while the composition in the
142 central part of the lens was buffered by replenishment (Stakes et al. 2006). However,
143 Cotsonika et al. (2005) proposed that dacitic melts might result from contamination of basaltic
144 resident melts by rhyolitic ones issued from the partial melting of the hydrated basaltic crust.
145 More recently, Wanless et al. (2010) suggested that MOR dacites result from extensive
146 fractional crystallization combined with partial melting and assimilation of amphibole-bearing
147 altered crust.

148

149 Past evolution documented by the Western Blanco Depression lavas

150

151 At the southern tip of the Cleft segment, the northern wall of the Western Blanco Depression
152 (Fig. 2a) provides a window through the slightly tectonized upper oceanic crust accreted for
153 1.4 Ma to the north of the ridge-transform intersection (Wilson et al. 1984; Embley and
154 Wilson 1992; Juteau et al. 1995; Karson et al. 2002b; Fig. 3a). A thick volcanic unit, made of
155 basaltic pillow-lavas, massive flows, and sparse feeder dikes (Juteau et al. 1995; Karson et al.
156 2002b), overlies an intensively hydrothermalized sheeted-dike complex (Manac'h et al. 1999).
157 The northern scarp provides an opportunity to study the temporal variations of the lava
158 composition by considering that the vertical succession of the lavas records increasing ages
159 with depth (Tivey et al. 1998; Pollock et al. 2005; Cordier et al. 2007; Fig. 3a).

160 Cordier et al. (2007) have shown that the lavas outcropping along the Northern Scarp
161 are mostly cogenetic. The conclusions of their petrological and geochemical study confirmed
162 that beneath the southern tip of the Cleft segment: (i) the melt evolution occurs in a complex
163 magma chamber, with differentiated, H₂O-rich compositions achieved in the cooler
164 solidification zones; (ii) the differentiation mainly results from fractional crystallization,
165 coupled with magma mixing between basaltic and intermediate melts; (iii) the mixing events
166 reveal the periodic recharge of the reservoir by mafic melts (Mg#=70) and this regime has
167 governed the magmatic system over the last ~1.4 Ma (Fig. 3b).

168 These results on the lavas erupted both at the present time (Smith et al. 1994; Stakes et
169 al. 2006) and over the last 1.4 Ma (Cordier et al. 2007) show that the magma chamber beneath
170 the southern end of the Cleft segment fulfills the conditions required to apply the model of
171 Rannou et al. (2006): (i) the chemical variations in the collected lavas derive from reservoir
172 differentiation and the chemical effects attributable either to the mantle source heterogeneity
173 or to variations of the melting degree can be considered negligible (Smith et al. 1994), except
174 perhaps for the dacite genesis (Wanless et al. 2010); (ii) the time evolution of the processes

175 occurring in the reservoir can be approached from the spatial distribution of the lava
176 chemistry, along the length of the Cleft segment (Fig. 2b) or vertically (Fig. 3b) along the
177 Northern Scarp (Smith et al. 1994; Pollock et al. 2005; Cordier et al. 2007); (iii) the magma
178 chamber has evolved in open system, with periodic melt inputs (Cordier et al. 2007).

179

180 **Geomathematical modeling of the temporal evolution of the magma chamber beneath** 181 **the southern Cleft segment**

182

183 Properties and resolution steps of the model

184

185 In the next sections, we will approach the variations of melt quantities and compositions
186 during the evolution of a periodically replenished and tapped steady-state magma chamber
187 through differential equations, by using the model developed by Rannou et al. (2006).

188 Incompatible trace elements (here rare earth elements) are especially suitable for such a
189 modeling. The behavior of compatible elements is too much dependent on both the nature and
190 the proportion of the fractionating minerals. The originality of the model comes from the use
191 of a sinusoidal function to reproduce the continuous and smoothed variations through time of
192 the quantity of melt refilling the reservoir. The volume of resident melt varies in response to
193 the intrusion and controls the crystallized and extruded volumes (Fig. 1a). Rannou et al.
194 (2006) showed that for a steady-state reservoir, the REE concentrations in melts expelled
195 from such a reservoir vary continuously through time following a sinusoidal curve.

196 Concentrations in incompatible elements are minimal just after the recharge of the system by
197 mafic melts, and they progressively increase due to the fractional crystallization occurring
198 between two recharge events. This approach reconciles both concepts about the open-system
199 magma chambers, usually treated separately: periodic inputs (O'Hara 1977; O'Hara and

200 Mathews 1981) and continuous inputs (De Paolo 1981; Reagan et al. 1987). Here, indeed, the
201 input is continuous but occurs at different rates.

202 Rannou et al. (2006) demonstrated that this model is especially suitable for modeling
203 the evolution of natural systems since it isolates the signals that are geologically significant.
204 For example, in a reservoir that is periodically recharged by melt of near constant
205 composition, the effects of natural disturbances in the replenishment cycles are strongly
206 attenuated and do not perturb significantly the calculated variation through time of the lava
207 composition (Rannou et al. 2006: their Fig. 3). Noises in the input function behave like a
208 high-frequency signal, attenuated by the magmatic system. In the same way, an occasional
209 and short variation of the incompatible trace element composition of the refilling melt,
210 traducing for instance a sudden wall-rock contamination, does not significantly modify the
211 modeled composition of the lavas that evolve in the system. For example, Rannou et al.
212 (2006) have considered a magmatic system assimilating a quantity of rocks (leucosome with
213 12 ppm Ce) corresponding to 10 % of the incoming melt (MORB with 3 ppm Ce) during a
214 fifth of the period. The difference in output Ce concentrations does not exceed 7% with
215 respect to the assimilation-free model: the lava concentration peak increases from 17.2 to 18.3
216 ppm of Ce just after the event, then to a damped value of 17.8 ppm at the following cycle.
217 These properties thus allow considering a smoothed, mathematically simple sinusoid to model
218 the magma recharge.

219 Rannou et al. (2006) divided the resolution procedure in two steps (Fig. 4). The
220 different parameters and their units are listed in Table 1. The first resolution step requires the
221 estimation of:

222 - the incompatible trace element concentrations in the cogenetic lavas that bound the
223 compositional range of the dataset, regarded as representative of the expelled liquids during
224 the open-system evolution of the reservoir (C_{\min}^E and C_{\max}^E for the element E, Table 1);

225 - the distribution coefficients between the global solid that crystallized and the melt
 226 (D^E);
 227 - the ratio between expulsion and crystallization rates (r_e).

228 We introduced an additional parameter with respect to the model of Rannou et al.
 229 (2006) to take into account the complexity of the differentiation in the composite magma
 230 chambers beneath the spreading ridges. Indeed, the interstitial residual melts of the crystal
 231 mush zones can be extracted and mix with the resident melt. The chemical evolution resulting
 232 from such a mechanism – if exists – certainly differs from the pure fractional crystallization
 233 process, as considered by Rannou et al. (2006). Thus, we considered the reinjection into the
 234 melt lens of a fraction f of interstitial liquid that has evolved within the partially solidified
 235 zones (Table 1). The equations are adapted from Langmuir (1989) by replacing the bulk
 236 distribution coefficient D^E by the parameter z^E (Table 1 and Eq. 2 of Fig. 4). As expressed, z^E
 237 models possible chemical exchanges between interstitial liquids and surrounding crystals
 238 (Langmuir 1989). Caroff (1995) named *imperfect fractional crystallization* this mechanism of
 239 solutal convection with mineralogical reactions, the principles of which being close to those
 240 of the *reactive crystallization* model of Collier and Kelemen (2010).

241 The different data are introduced into Eq. 1 of Fig. 4, in which all the parameters are
 242 considered constant through time. In a first step, for each REE, we run iteratively the Eq. 1
 243 with different values of C_i^E and β^E (internal parameter, see Table 1 and Rannou et al. 2006)
 244 until the maximum and minimum concentrations that are modeled match those measured in
 245 lavas (Rannou et al. 2006). The replenishment pulsation (ω) is arbitrarily fixed for this first
 246 step as it has no effect on the calculated C^E values. This is equivalent to model the variations
 247 of C^E in function of a dimensionless time. The REE concentrations in the replenishment melt
 248 (C_i^E) and the β^E value for each REE are estimated. The average of the β^E values calculated for
 249 all the considered REE (β_{av}) corresponds to the ratio between the replenishment pulsation and

250 the crystallization rate (Table 1). The good reproducibility of the β^E values, i.e. a low standard
 251 deviation on their average $\sigma(\beta_{av})$, is then used to validate the set of distribution coefficients.

252 The second step of the modeling requires the estimation of the mean rate of melt
 253 injection $[q_i]$ into the reservoir and of the variation of the quantity (here expressed as volume)
 254 of resident melt during a cycle ($Q_{max}-Q_{min}$). These parameters are introduced in Eqs. 3-5 (Fig.
 255 4), together with r_e and β_{av} , to calculate the fraction of melt crystallized by year (α), the
 256 period of the replenishment (T), and the mean residence time of the melt within the reservoir
 257 (τ). By introducing these results in Eq. 6 (Fig. 4), we model the temporal variations of the
 258 resident melt volume.

259 The curves of Fig. 5 illustrate the effects of the variation of some parameters
 260 introduced into the modeling ($C_{max}^E, f, Q_{max}-Q_{min}$) on the calculated compositions of melt
 261 expelled from the periodically recharged reservoir (from Eq. 1: Fig. 5a, b) and on the volumes
 262 of resident melt (from Eq. 6: Fig. 5c, d).

263

264 Procedure applied to the magma system beneath the southern Cleft segment

265

266 *Model parameter estimation*

267

268 Our calculations are only based on rare earth elements (REE) because (i) these elements have
 269 been extensively analyzed in the available samples, (ii) their concentrations have not been
 270 significantly modified during subsequent seawater alteration, and (iii) their individual
 271 mineral/liquid distribution coefficients are quite well constrained from literature data. Along
 272 the Northern Scarp, Cordier et al. (2007) defined a cogenetic suite that extends from the mafic
 273 basalt BV2960-7 (MgO~8.1 wt.%) to the ferrobasalt BN02-12 (MgO~4.32 wt.%), both
 274 aphyric (Figs 2c and 6). We used these two samples to approach C_{min}^E and C_{max}^E , respectively

275 (Table 2). However, Cordier et al. (2007) found that some ferrobasalts might result from
 276 mixing between dacitic residual melts (MgO~1.1 wt.%) and mafic melts (MgO~8.5 wt.%).
 277 Even if such a hypothesis is judged unlikely in recent studies, such as Wanless et al. (2010), a
 278 second set of calculations has been performed using a more evolved C_{\max}^E end-member, in
 279 view to test the response of the model to a variation of the chemical parameters introduced
 280 into Eq. 1 of Fig. 4. All along the south Cleft segment, the only dacitic glass has been sampled
 281 by Stakes et al. (2006) but has not been analyzed for REE by these authors (Table 2, Fig. 2,
 282 sample RC10). Consequently, we used the composition of an andesite collected on the
 283 Galapagos Spreading Center (Fornari et al. 1983; Perfit et al. 1983), that has REE pattern
 284 parallel to the Northern Scarp ferrobasalts (Table 2 and Fig. 6a).

285 The next parameter, r_e (Table 1), has been approximated following the method
 286 proposed by Rannou et al. (2006) as the ratio between the thicknesses of the basaltic and
 287 gabbroic layers of the oceanic crust (Figs. 1b and c). Assuming that the gabbros extend from
 288 the seismically imaged melt lens to the Moho, the ratio of the melt lens depth (2 km, Canales
 289 et al. 2005) to the thickness of the plutonic complex (5 km, West et al. 2003) provides a r_e
 290 ratio equal to 0.4.

291 The REE bulk distribution coefficients have been calculated by weighting the
 292 individual mineral/liquid distribution coefficients of the mineral phases (Agee 1990; Fujimaki
 293 et al. 1984) by their appropriate proportion in the global crystallizing assemblage. For a
 294 differentiation leading to ferrobasalts, the phase proportions are determined for a Fe-Ti oxide-
 295 free gabbroic cumulate (D_1^E , Table 2). For an andesitic term, the crystallizing assemblage
 296 includes Fe-Ti oxides, as suggested by the drastic drop in the TiO_2 content observed in the
 297 Fig. 3 diagram, and apatite (D_2^E , Table 2).

298 By varying the f value from 0 to 1, we can describe all the cases ranging from perfect
 299 equilibrium (restricted to the solidification zone) to perfect fractional crystallization. The

300 procedure described by Rannou et al. (2006) presupposes a f value equal to 1 ($z^E=D^E$). In our
301 calculations, we also tested the model with a value of f of 0.5.

302 The last parameters to be estimated are the melt quantities, here expressed as volumes.
303 Beneath the Cleft segment, the distribution of the axial crustal reflector imaging the melt lens
304 shows that the magma chamber is continuous over 5 to 10 km-long intervals, even if its
305 characteristics (depth and crystallinity) vary with shorter wavelength (Canales et al. 2005). It
306 is likely that the scale of the magma chamber segmentation has not changed significantly over
307 the last thousands of years. Thus, we calculated the different melt volumes introduced in the
308 model resolution by considering a 10-km long magma chamber.

309 The mean rate of melt injection [q_i] is regarded as the volume of crust accreted per
310 year. For a 7 km-thick crust (West et al. 2003) and a full spreading rate of 56 mm/yr (Wilson
311 1993), [q_i] is equal to $0.004 \text{ km}^3/(\text{yr}.10\text{km})$.

312 The variation of the volume of resident melt during a cycle ($Q_{\max}-Q_{\min}$) is the least
313 precisely estimated, because it requires assumptions on the quantity of melt expellable from
314 the magmatic system and thus on the melt distribution over the crust thickness beneath the
315 ridge axis. Beneath the southern part of the Cleft segment, given the lens size and crystallinity
316 deduced from seismic data (Canales et al. 2005, 2006), the quantity of melt that can be
317 expelled from the uppermost, seismically imaged and partially crystallized lens (gabbro
318 glacier model GG1, Fig. 1b) during the time interval of inflation and deflation of the magma
319 chamber is ca. 0.45 km^3 (Table 3). We also run the calculations with a higher volume of melt
320 ($0.63 \text{ km}^3/10 \text{ km}$, GG2, Fig. 1b and Table 3) to consider the partial draining of the interstitial
321 melt from the mushy solidification zones to the melt lens during compaction of the magma
322 chamber (Lagabrielle and Cormier 1999). Finally, we made an attempt to estimate the volume
323 of melt expellable from several sheeted sills distributed all over the crust thickness (SS model,
324 Fig. 1c). However, no geophysical results can be actually used to decide how many sills lie in

325 depth and how these sills contribute to the magma chamber tapping. We arbitrarily considered
326 that no more than a second melt lens is affected by the melt tapping, assigning a value of 0.9
327 $\text{km}^3/10 \text{ km}$ to the parameter $Q_{\text{max}}-Q_{\text{min}}$ (Table 3).

328

329 *Results*

330

331 The geochemical and temporal results of the modeling applied to the magma system beneath
332 the southern Cleft segment are shown in Table 3 and in Figs 5-6. The consistency of the set of
333 D^E (and z^E) coefficients, and consequently the validity of the calculated C_i^E , is attested by the
334 good reproducibility of the β^E values calculated for the different REE (Table 3), as shown by
335 the low $\sigma(\beta_{\text{av}})$ values (ranging from 0.119 to 0.200, Table 3). For a f value of 1, the C_i^E values
336 calculated from the ferrobasalt and andesite composition to approach C_{max}^E are fairly similar
337 (Table 3 and Fig. 6b). The C_i^E patterns have lower REE contents and are slightly more
338 depleted in light REE relative to lavas. The pattern of the primary melt with $\text{Mg}\#=70$
339 determined by Cordier et al. (2007) is very close to and bracketed by the two theoretical
340 refilling melt compositions (Fig. 6b). This similarity confirms that the modeled replenishment
341 liquid can be regarded as a primary melt.

342 The differentiation sequence leading to andesites cannot be reproduced using a low f
343 value to model a low melt flow from the solidification zones to the main magma lens
344 (Langmuir 1989, Caroff 1995). Indeed, for most of the REE (except La and Nd), the modeled
345 composition of expelled melts does not match the observed composition range. This result
346 might support that andesite/dacite compositions cannot be achieved by pure MORB fractional
347 crystallization, consistently with the Wanless et al. (2010) conclusions. For the differentiation
348 leading to ferrobasalts, introducing a f value of 0.5 results in C_i^E values slightly higher than

349 for perfect fractional crystallization ($f=1$, Fig. 5b), without significant increase of the β^E
350 variability ($\sigma(\beta_{av})=0.124$, Table 3).

351 When calculating the temporal data, the only varying parameters are β_{av} and $Q_{max}-Q_{min}$
352 (Eqs 3-5, Fig. 4). Low β_{av} , resulting either from high C_{max}^E or from low f values (Table 1,
353 Step 1), produces high average crystallization rate α , high replenishment period T , and low
354 average melt residence time τ (Fig. 5a, b and Table 3, Step 2). Conversely, an increase of the
355 variation of the magma chamber volume during a cycle ($Q_{max}-Q_{min}$) results in a diminution of
356 α and an increase of both T and τ (Fig. 5c, d and Table 3, Step 2). Thus, considering a
357 reservoir with a well-established thermal regime, the more the volume of interconnected (i.e.
358 expellable) liquids is high the more the time required for magma differentiation is long. As
359 the temporal results are very sensitive to the $Q_{max}-Q_{min}$ value (Fig. 5 and Table 3), they
360 strongly depend on the assumptions about the quantity of expellable melt.

361 The volume of melt in the reservoir oscillates through time with inflation plus
362 deflation cycles of 550 to 2250 years, in function of the values ascribed to the chemical and
363 geological parameters (Table 3 and Fig. 5). In average, melts reside 60 to 150 years in the
364 magma chamber (Table 3). The variation range of the calculated magma residence times is
365 close to that determined using Ra-Th disequilibria (tens to thousands years) for basaltic to
366 andesitic magmas that have evolved in steady-state, well mixed, open-reservoirs (Pyle 1992).
367 However, the temporal results of this modeling can hardly be validated by direct comparison
368 with radiochronological data measured on the studied samples. First, we cannot estimate the
369 cycle period by dating the mafic samples that bracket a chemical cycle. Current datation
370 methods have not a sufficient time resolution (e.g. magnetic isochrones, Fig. 3), they are
371 difficult to apply to tholeiites (e.g. K/Ar and $^{40}\text{Ar}/^{39}\text{Ar}$ methods), or they are not suitable for
372 the considered lavas that are older than about 300 Ka (e.g. $^{230}\text{Th}/^{238}\text{U}$, Fig. 2). Second, our
373 samples are too old ($> 8,000$ years) to still record the $^{226}\text{Ra}-^{230}\text{Th}$ or $^{210}\text{Pb}-^{226}\text{Ra}$ disequilibria,

374 which are generally used to estimate the magma residence time in spreading ridge context
375 (Cooper et al. 2003; Goldstein et al. 1993; Rubin and MacDougall 1990; Rubin et al. 2005;
376 Volpe and Goldstein 1993).

377

378 **Conclusions**

379

380 In this study, we attempted to model the time evolution of the periodically recharged magma
381 chamber beneath the southern tip of the Cleft spreading segment. First, Rannou et al. (2006)
382 developed a realistic mathematical procedure to model the geochemical evolution of changing
383 volume magma chambers, periodically recharged and tapped. Subsequently, in their study on
384 the lavas exposed along the northern wall of the Western Blanco Depression, Cordier et al.
385 (2007) highlighted a complex chemical evolution with depth, interpreted as the result of
386 periodic replenishment of the southernmost magma reservoir of the Cleft segment.

387 We applied here the procedure of Rannou et al. (2006) to this zone of the Cleft
388 segment. The composition of the replenishment melt that we modeled is consistent with that
389 obtained from mineralogical and chemical data for a $Mg\#=70$ melt (Cordier et al. 2007). This
390 reproducibility between theoretical and experimental compositions, already shown by Rannou
391 et al. (2006) in their application to North Fiji Basin lavas, validates the first step of the
392 modeling. In addition, by introducing geological parameters in the modeling procedure, we
393 estimated that the magma chamber is refilled every $1,100 \pm 500$ years and that the melt
394 resides ~ 100 years within the reservoir beneath the southern Cleft segment. These temporal
395 results are close to those calculated in a same way for the ultra-fast spreading East Pacific
396 ridge (period $T = 750$ years and magma residence time $\tau = 300$ years; Rannou et al. 2006).

397 This study demonstrates the applicability of the model of Rannou et al. (2006) to
398 magma reservoirs beneath spreading ridges. Once the periodic evolution of the magma

399 chamber demonstrated, it can be used to approach the composition of the replenishment melt.
400 Besides, its application to sites where conventional dating methods are not relevant is an
401 auxiliary approach to access the periodicity of the magmatic cycles and the melt residence
402 time. The result accuracy depends on the precision when estimating the variable parameters,
403 from geological and geochemical data. Inversely, for sites where our theoretical approach
404 could be combined with radiochronological data, such a combination could bring new
405 constraints on some of the data used for the model resolution and consequently on the
406 subjacent assumptions about the magma system. For example, the volume of melt expellable
407 from the magmatic system ($Q_{\max}-Q_{\min}$) could then be stated and the models of lower oceanic
408 crust accretion be discriminated.

409
410 *Acknowledgments:* We acknowledge Johann G. Raith for editorial assistance and Wendy
411 Bohrson for reviewing this work.

413 **References**

- 414
415 Agee CB (1990) A new look at differentiation of the Earth from melting experiments on the
416 Allende meteorite. *Nature*, 346: 834-837
- 417 Boudier F, Nicolas A, Ildefonse B (1996) Magma chambers in the Oman ophiolite: Fed from
418 the top or from the bottom? *Earth and Planetary Science Letters* 144: 239-250
- 419 Canales JP, Detrick RS, Carbotte SM, Kent GM, Diebold JB, Harding AJ, Babcock JM,
420 Nedimovic MR, Van Ark E (2005) Upper crustal structure and axial topography at
421 intermediate spreading ridges: Seismic constraints from the southern Juan de Fuca
422 ridge. *Journal of Geophysical Research*, 110, B12104, doi: 10.1029/2005JB003630

- 423 Canales JP, Singh SC, Detrick RS, Carbotte SM, Harding AJ, Kent GM, Diebold JB, Babcock
424 JM, Nedimovic MR (2006) Seismic evidence for variations in axial magma chamber
425 properties along the southern Juan de Fuca Ridge. *Earth and Planetary Science Letters*
426 246: 353-366
- 427 Caroff M (1995) Open system crystallization and mixing in two-layers magma chambers.
428 *Lithos* 36: 85-102
- 429 Caroff M, Fleutelot C (2003) The north-south propagating spreading center of the North Fiji
430 Basin. Modeling of the geochemical evolution in periodically replenished and tapped
431 magma chambers. *Mineralogy and Petrology* 79: 203-224
- 432 Chadwick W, Embley, RW (1998) Graben formation associated with recent dike intrusions
433 and volcanic eruptions on the mid-ocean ridge. *Journal of Geophysical Research* 103:
434 9807-9825
- 435 Collier ML, Kelemen PB (2010) The case for reactive crystallization at Mid-Ocean Ridges.
436 *Journal of Petrology* 51: 1913-1940
- 437 Cooper KM, Goldstein SJ, Sims KWW, Murrell MT (2003) Uranium-series chronology of
438 Gorda ridge volcanism: new evidence from the 1996 eruption. *Earth and Planetary*
439 *Science Letters* 206: 459-475
- 440 Cordier C, Caroff M, Juteau T, Fleutelot C, Hémond C, Drouin M, Cotten J, Bollinger C
441 (2007) Bulk-rock geochemistry and plagioclase zoning in lavas exposed along the
442 northern flank of the Western Blanco Depression (Northeast Pacific): Insight into
443 open-system magma chamber processes. *Lithos* 99: 289-311
- 444 Cotsonika LA, Perfit MR, Smith MC, Kamenov GD, Stakes DS, Ridley WI, Wallace P (2005)
445 The occurrence and origin of andesites and dacites from the Southern Juan de Fuca
446 Ridge. *Eos Transactions, American Geophysical Union, Fall Meeting Supplement* 86
447 (18), Abstract V13A-04

- 448 Davis AS, Clague DAC., Cousens BL, Keaten B, Paduan JB (2008) Geochemistry of basalt
 449 from the North Gorda segment of the Gorda Ridge: Evolution toward ultraslow
 450 spreading ridge lavas due to decreasing magma supply. *Geochemistry Geophysics*
 451 *Geosystems* 9, Q04004, doi: 10.1029/2007GC001775
- 452 De Paolo DJ (1981) Trace element and isotopic effects of combined wallrock assimilation and
 453 fractional crystallization. *Earth and Planetary Science Letters* 53: 189-202
- 454 Detrick RS, Buhl P, Vera EE, Mutter JC, Orcutt JA, Madsen JA, Brocher TM (1987)
 455 Multichannel seismic imaging of a crustal magma chamber along the East Pacific
 456 Rise. *Nature* 326: 35-41
- 457 Einaudi F, Godard M, Pezard PA, Cochemé JJ, Coulon C, Brewer T, Harvey P (2003)
 458 Magmatic cycles and formation of the upper oceanic crust at spreading centers:
 459 Geochemical study of a continuous extrusive section in the Oman ophiolite.
 460 *Geochemistry Geophysics Geosystems* 4, 8608, doi: 10.1029/2002GC000362
- 461 Embley RW, Wilson DS (1992) Morphology of the Blanco Transform Fault Zone-NE Pacific:
 462 Implications for its tectonic evolution. *Marine Geophysical Researches* 14: 25-45.
- 463 Fornari DJ, Perfit MR, Malahoff A, Embley RW (1983) Geochemical studies of abyssal lavas
 464 recovered by DSRV Alvin from eastern Galapagos rift, Inca transform and Ecuador
 465 rift 1. Major element variations in natural glasses and spacial distribution of lavas.
 466 *Journal of Geophysical Research* 88: 10519-10529
- 467 France L, Koepke J, Ildefonse B, Cichy SB, Deschamps F (2010) Hydrous partial melting in
 468 the sheeted dike complex at fast spreading ridges: experimental and natural
 469 observations. *Contributions to Mineralogy and Petrology* 160: 683-704
- 470 Fujimaki H, Tatsumoto M, Aoki KI (1984) Partition coefficients of Hf, Zr, and REE between
 471 phenocrysts and groundmasses. Lunar and Planetary Science Conference, 14th,
 472 Houston, TX, *Journal of Geophysical Research, Supplement* 89, B662-B672

- 473 Garrido C, Kelemen P, Hirth G (2001) Variation of cooling rate with depth in lower crust
474 formed at an oceanic spreading ridge: Plagioclase crystal size distributions in gabbros
475 from the Oman ophiolite. *Geochemistry Geophysics Geosystems* 2, 1041, doi:
476 10.1029/2000GC000136
- 477 Gillis KM, Coogan LA (2002) Anatectic migmatites from the roof of an ocean ridge magma
478 chamber. *Journal of Petrology* 43: 2075-2095
- 479 Goldstein SJ, Murrell MT, Williams RW (1993) ^{231}Pa and ^{230}Th chronology of mid-ocean
480 ridge basalts. *Earth and Planetary Science Letters* 115: 151-159
- 481 Henstock TJ (2002) Compaction control of melt distribution at fast-spreading mid-ocean
482 ridges. *Geophysical Research Letters* 29, 1137, doi: 10.1029/2001GL013755
- 483 Henstock TJ, Woods AW, White RS (1993) The accretion of oceanic crust by episodic sill
484 intrusion. *Journal of Geophysical Research* 98: 4143-4161
- 485 Hooft EEE, Detrick RS, Kent GM (1997) Seismic structure and indicators of magma budget
486 along the Southern East Pacific Rise. *Journal of Geophysical Research* 102: 27319-
487 27340
- 488 Hussenoder SA, Collins JA, Kent GM, Detrick RS (1996) Seismic analysis of the axial
489 magma chamber reflector along the southern East Pacific Rise from conventional
490 reflection profiling. *Journal of Geophysical Research* 101: 22087-22105
- 491 Juteau T et al (1995) A submersible study in the Western Blanco Fracture Zone, N.E. Pacific:
492 structure and evolution during the last 1.6 Ma. *Marine Geophysical Researches* 17:
493 399-430
- 494 Karson JA et al (2002a) Structure of uppermost fast spread oceanic crust exposed at the Hess
495 Deep Rift: Implications for subaxial processes at the East Pacific Rise. *Geochemistry
496 Geophysics Geosystems* 3, 1002, doi: 10.1029/2001GC000155

- 497 Karson JA, Maurice AT, Delaney JR (2002b) Internal structure of uppermost oceanic crust
498 along the Western Blanco Transform Scarp: Implications for subaxial accretion and
499 deformation at the Juan de Fuca Ridge. *Journal of Geophysical Research* 107, 2181,
500 doi: 10.1029/2000JB000051
- 501 Kelemen PB, Koga KT, Shimizu N (1997) Geochemistry of gabbro sills in the crust/mantle
502 transition zone of the Oman ophiolite: Implications for the origin of the oceanic lower
503 crust. *Earth and Planetary Science Letters* 146: 475-488
- 504 Koepke J, Christie DM, Dziony W, Holtz F, Lattard D, MacLennan J, Park S, Scheibner B,
505 Yamasaki T, Yamasaki S (2008) Petrography of the dike-gabbro transition at IODP
506 Site 1256 (equatorial Pacific): The evolution of the granoblastic dikes. *Geochemistry
507 Geophysics Geosystems* 9: Q07O09, doi: 10.1029/2008GC001939
- 508 Korenaga J, Kelemen PB (1998) Melt migration through the oceanic lower crust: A constraint
509 from melt percolation modelling with finite solid diffusion. *Earth and Planetary
510 Science Letters* 156: 1-11
- 511 Lagabrielle Y, Cormier M-H (1999) Formation of large summit troughs along the East Pacific
512 Rise as collapse calderas: An evolutionary model. *Journal of Geophysical Research*
513 104: 12971-12988
- 514 Langmuir CH (1989) Geochemical consequence of in situ crystallization. *Nature* 340: 199-
515 205
- 516 Manac'h G, Lécuyer C, Juteau T (1999) A fluid inclusion and stable isotope study of
517 hydrothermal circulation in a transform zone: Western Blanco Depression, northeast
518 Pacific. *Journal of Geophysical Research* 104: 12941–12970
- 519 Normark WR, Morton JL, Koski R, Clague DA (1983) Active hydrothermal vents and sulfide
520 deposits on the southern Juan de Fuca Ridge. *Geology* 11: 158-163

- 521 O'Hara MJ (1977) Geochemical evolution during fractional crystallization of a periodically
522 refilled magma chamber. *Nature* 266: 503-507
- 523 O'Hara MJ, Mathews RE (1981) Geochemical evolution in an advancing, periodically
524 replenished, periodically tapped, continuously fractionated magma chamber. *Journal*
525 *of the Geological Society of London* 138: 237-277
- 526 Pallister JS, Hopson CA (1981) Samail Ophiolite plutonic suite: Field relations, phase
527 variation, cryptic variation and layering, and a model of a spreading ridge magma
528 chamber. *Journal of Geophysical Research* 86: 2593-2644
- 529 Perfit MR, Fornari DJ, Malahoff A, Embley RW (1983) Geochemical studies of abyssal lavas
530 recovered by DSRV ALVIN from Eastern Galapagos Rift, Inca Transform, and
531 Ecuador Rift, 3, Trace element abundances and petrogenesis. *Journal of Geophysical*
532 *Research* 88: 10551-10572
- 533 Phipps Morgan J, Chen YJ (1993) The genesis of oceanic crust: Magma injection,
534 hydrothermal circulation, and crustal flow. *Journal of Geophysical Research* 98: 6283-
535 6297
- 536 Pollock MA, Klein EM, Karson JA, Tivey MA (2005) Temporal and spacial variability in the
537 composition of lavas exposed along the Western Blanco Transform Fault.
538 *Geochemistry Geophysics Geosystems* 6, Q11009, doi: 10.1029/2005GC001026
- 539 Pyle DM (1992) The volume and residence time of magma beneath active volcanoes
540 determined by decay-series disequilibria methods. *Earth and Planetary Science Letters*
541 112: 61-73
- 542 Quick JE, Denlinger RP (1993) Ductile deformation and the origin of layered gabbro in
543 ophiolites. *Journal of Geophysical Research* 98: 14015-14027

- 544 Rannou E, Caroff M, Cordier C (2006) A geochemical approach to model periodically
545 replenished magma chambers: Does oscillatory supply account for the magmatic
546 evolution of EPR 17-19°S? *Geochimica et Cosmochimica Acta* 70: 4783-4796
- 547 Reagan MK, Gill JB, Malavassi E, Garcia MO (1987) Changes in magma composition at
548 Arenal volcano, Costa Rica, 1968-1985 : real-time monitoring of open-system
549 differentiation. *Bulletin of Volcanology* 49: 415-434
- 550 Rubin KH, MacDougall JD (1990) Dating of neovolcanic MORB using ($^{226}\text{Ra}/^{230}\text{Th}$)
551 disequilibrium. *Earth and Planetary Science Letters* 101: 313-322
- 552 Rubin KH, van Der Zander I, Smith MC, Bergmanis EC (2005) Minimum speed limit for
553 ocean ridge magmatism from ^{210}Pb – ^{226}Ra – ^{230}Th disequilibria. *Nature* 437: 534-538
- 554 Singh SC, Kent GM, Collier JS, Harding AJ, Orcutt JA (1998) Melt to mush variations in
555 crustal magma properties along the ridge crest at the southern East Pacific Rise.
556 *Nature* 394: 874-878.
- 557 Sinton JM, Detrick RS (1992) Mid-Ocean Ridge Magma Chambers. *Journal of Geophysical*
558 *Research* 97: 197-216
- 559 Smewing JD (1981) Mixing characteristics and compositional differences in mantle-derived
560 melts beneath spreading axes: evidence from cyclically layered rocks in the ophiolite
561 of north Oman. *Journal of Geophysical Research* 86: 2645-2659
- 562 Smith MC, Perfit MR, Jonasson IR (1994) Petrology and geochemistry of basalts from the
563 southern Juan de Fuca ridge: Controls on the spatial and temporal evolution of mid-
564 ocean ridge basalt. *Journal of Geophysical Research* 99: 4787-4812
- 565 Stakes DS, Perfit MR, Tivey MA, Caress DW, Ramirez TM, Maher N (2006) The Cleft
566 revealed: Geologic, magnetic, and morphologic evidence for construction of upper
567 oceanic crust along the southern Juan de Fuca Ridge. *Geochemistry Geophysics*
568 *Geosystems* 7, Q04003, doi: 10.1029/2005GC001038

- 569 Tivey MA (1996) Vertical magnetic structure of ocean crust determined from near-bottom
570 magnetic field measurements. *Journal of Geophysical Research* 101: 20275-20296
- 571 Tivey MA, Johnson HP, Fleutelot C, Hussenoeder SA, Lawrence R, Waters C, Wooding, B
572 (1998) Direct measurement of magnetic reversal polarity boundaries in a cross-section
573 of oceanic crust. *Geophysical Research Letters* 25: 3631-3634
- 574 Volpe AM, Goldstein SJ (1993) ^{226}Ra - ^{230}Th disequilibrium in axial and off-axis mid-ocean
575 ridge basalts. *Geochimica et Cosmochimica Acta* 57: 1233-1241
- 576 Wanless VD, Perfit MR, Ridley WI, Klein E (2010) Dacite petrogenesis on Mid-Ocean
577 Ridges: Evidence for oceanic crustal melting and assimilation. *Journal of Petrology*
578 51: 2377-2410
- 579 West M, Menke W, Tolstoy M (2003) Focused magma supply at the intersection of the Cobb
580 hotspot and the Juan de Fuca ridge. *Geophysical Research Letters* 30: 1724
- 581 Wilson DS (1993) Confidence intervals for motion and deformation of the Juan de Fuca plate.
582 *Journal of Geophysical Research* 98: 16053-16071
- 583 Wilson DS, Hey RN, Nishimura C (1984) Propagation as a mechanism of reorientation of
584 Juan de Fuca Ridge. *Journal of Geophysical Research* 89: 9215-9225
- 585 Wilson DS et al (2006) Drilling to gabbro in intact ocean crust. *Science* 312: 1016-1020.

586

587 **Figure captions:**

588

589 Figure 1. Theoretical magma chamber considered in the mathematical modeling (a) and its
590 adaptation to fit with the different mechanisms proposed for the accretion of the lower
591 oceanic crust and for the related geometry of the magma chamber beneath fast to intermediate
592 spreading ridges (b and c). In the “Gabbro glacier” model (b), crystallization takes place in a
593 thin sill at the base of the sheeted dike complex from which cumulates subside down

594 (Henstock 2002; Henstock et al. 1993; Phipps Morgan and Chen 1993; Quick and Denlinger
 595 1993). GG1 and GG2 refer to the two scenarios envisioned when discussing in the text the
 596 volume of melt expellable from the reservoir (with or without the contribution of the
 597 interstitial melt of the crystal mush, respectively). In the “Sheeted sill” model (c), the lower
 598 oceanic crust is formed through *in situ* crystallization of multiple sills (Boudier et al. 1996;
 599 Garrido et al. 2001; Kelemen et al. 1997; Korenaga and Kelemen 1998). The volume of
 600 expellable melt is then approached by considering the contribution of two melt lenses. The
 601 different parameters are defined in Table 1: Q refers to melt volumes, C to element
 602 concentrations, and the subscripts i , c and e to injected, crystallized and expelled,
 603 respectively. The wide arrows show the main melt fluxes through the magmatic system.

604
 605 Figure 2. Chemical evolution of the lavas collected along the Cleft segment and the Northern
 606 Scarp of the Western Blanco Depression (WBD). a) Shaded relief bathymetry of the Cleft
 607 segment and WBD with the location of the submersible dives along the Northern Scarp
 608 (Cordier et al. 2007; Juteau et al. 1995) and of the Cleft segment samples (Smith et al. 1994;
 609 Stakes et al. 2005). Inset: location map of the WBD in the NE Pacific. JdF R.: Juan de Fuca
 610 ridge; G. R.: Gorda ridge; BTF: Blanco Transform Fault. b) Evolution of the MgO contents in
 611 lavas with latitude. c) TiO_2 versus MgO diagram. Samples used in the model resolution are
 612 labeled and their composition is listed in Table 2. Chemical data are from the literature (Smith
 613 et al. 1994; Stakes et al. 2005; Cordier et al., 2007).

614
 615 Figure 3. Chemical evolution with depth in the extrusive unit of the Northern Scarp for two
 616 groups of dives, located ca. 25 and 40 km eastward from the Juan de Fuca axis, respectively.
 617 a) Lithologies observed along the Northern Scarp superimposed on the magnetic cross section
 618 (Tivey 1996; Tivey et al. 1998). Normal polarity crust is shaded in light gray (M: Matuyama)

619 and inverse polarity crust in dark gray (B: Brunhes, J: Jaramillo, 2: Anomaly 2). The filled
 620 stars show the position of the dives illustrated in b). b) Variations of La with depth. They are
 621 consistent with those of Mg# shown in Cordier et al. (2007) (their Fig, 10). The changes from
 622 mafic (low La contents) to intermediate or evolved terms (high La contents) are thought to
 623 result from fractional crystallization, followed by returns to mafic compositions during
 624 replenishment events.

625

626 Figure 4. Resolution procedure of the model of Rannou et al. (2006). Parameters are defined
 627 in Table 1. In the step 1, Eq. 1 is modified after Eq. 12 of Rannou et al. (2006). ω is fixed
 628 arbitrarily to 2π . f and z^E are new parameters with respect to the model of Rannou et al. (2006)
 629 and are used to model the mixing between the interstitial residual melts of the crystal mush
 630 zones and the melt residing in the lens.

631

632 Figure 5. Effect of the variation of the parameters C_{\max}^E , f and $Q_{\max}-Q_{\min}$ on the REE
 633 concentration in lavas (a and b) and on the resident melt volume (c and d). La is shown as an
 634 example of the REE concentrations in lavas. The curves are drawn using Eq. 1 and Eq. 6 (Fig.
 635 4). The parameters C_{\min}^{La} ($3.1 \mu\text{g/g}$), r_e (0.4) and $[q_i]$ ($0.004 \text{ km}^3/\text{yr} \cdot 10\text{km}$) are similar in the
 636 different illustrated cases. The values of f , C_{\max}^E and $Q_{\max}-Q_{\min}$ used in each case are stated
 637 on the figure. f is the fraction of interstitial melt migrating from the solidification zone into the
 638 melt lens. $f=1$ when the melt lens collects the entire volume of the melts that have evolved in
 639 the solidification zones (perfect fractional crystallization). $f=0.5$ when half of the melts that
 640 have evolved in the solidification zones are injected within the melt lens. The results for each
 641 calculation are listed in Table 3. The model does not give suitable solution for $f=0.5$ and
 642 $C_{\max}^{\text{La}} = 20.6 \mu\text{g/g}$ (b).

643

644 Figure 6. Chemical compositions used for the model resolution and results of the first step of
645 the modeling. (a) The range of REE compositions of the Northern Scarp lavas, the C_{\min}^E and
646 C_{\max}^E used in the modeling (listed in Table 2) and the Mg#70 melt composition deduced by
647 Cordier et al. (2007) from petrological and geochemical data are shown. (b) Composition of
648 the replenishment melt (C_i^E , Table 3) together with the lava range (see text). C_i^E are calculated
649 graphically for each REE by introducing into Eq. 1 of Fig. 4 the following parameters: $r_e =$
650 0.4; $C_{\max}^E =$ REE contents in Fe-basalt and andesite, respectively (Table 2); $f=0.5$ and $f=1$.
651 The theoretical C_i^E patterns have lower REE contents than the lavas and are slightly more
652 depleted in LREE. The spectrum of the Mg#=70 primary melt is very close to and bracketed
653 by our theoretical refilling melts. The model does not give suitable C_i^E pattern for $f = 0.5$ and
654 C_{\max}^E (andesite).

655

Table 1. Definition of the model parameters.

Parameters	Values ^a	Definition
C_{\max}^E ($\mu\text{g/g}$)	Table 2	Concentration of the rare earth element E in the most evolved lava
C_{\min}^E ($\mu\text{g/g}$)	Table 2	Concentration of E in the most mafic lava
C_r^E ($\mu\text{g/g}$)	Table 2	Concentration of E in the refilling melt
D^E	Table 2	Bulk distribution coefficient of E
f^b	0.5 and 1	Fraction of melt evolving in the solidification zones and reintroduced in the melt lens
$z^{E b}$	Table 2	Coefficient accounting for melt differentiation due to fractional crystallization and possible chemical exchanges between melt and crystals in crystal mush
$[q_i]$ ($\text{km}^3/\text{yr} \cdot 10\text{km}$) ^c	0.004	Average rate of melt input in the reservoir
α (yr^{-1})		Average crystallization rate: fraction of melt crystallized per time unit
$\omega/2\pi$ (Hz)		Frequency of the replenishment, with ω the pulsation of the replenishment
β^E		Internal parameter iteratively estimated for each E, the average of which gives β_{av}
β_{av}		Ratio between pulsation (ω) and crystallization rate (α), average of the β^E values
r_e	0.4	Mean ratio between average extrusion and crystallization rates
Q ($\text{km}^3/\text{yr} \cdot 10\text{km}$) ^c		Volume of melt residing (i.e. expellable) in the reservoir
$Q_{\max}-Q_{\min}$ ($\text{km}^3/10\text{km}$) ^c	0.45 to 0.90	Amplitude of the variations of the melt volume in the reservoir
T (yr)		Period of the replenishment
τ (yr)		Average magma residence time

^a Values introduced into the resolution procedure are stated here when constant for the different REEs. Otherwise, they are listed in Table 2.

^b Parameters adapted from the equations of *in situ* crystallization of Langmuir (1989).

^c Units are expressed for a 10 km-long magma chamber, as typically observed beneath the Cleft segment. See text.

Table 2. Chemical input parameters.

Sample	2960-7	BN02-12	999-1B	RC-10				
Parameter ^a	C_{\min}^E	C_{\max}^E	C_{\max}^E		z_1^{Eb}	z_2^{Eb}	z_1^{Eb}	z_2^{Eb}
Type ^c	Bas.	Fe-bas.	And.	Dac.	→Fe-bas.	→And.	→Fe-bas.	→And.
f					1	1	0.5	0.5
Loc. ^d	NS	NS	Galap.	Cleft				
Analysis ^e	WR	WR	GL	GL				
Ref. ^f	1	1	2	3				
SiO ₂ (wt. %)	49.50	48.85	56.70	63.15				
TiO ₂	1.36	3.61	1.91	1.29				
Al ₂ O ₃	15.15	11.62	11.42	12.47				
Fe ₂ O ₃ ^{tot g}	10.80	19.10	17.98	11.84				
MnO	0.19	0.26	0.29	0.18				
MgO	8.05	4.27	1.80	1.13				
CaO	12.00	7.78	6.90	4.52				
Na ₂ O	2.30	3.10	3.48	4.43				
K ₂ O	0.15	0.34	0.39	0.98				
P ₂ O ₅	0.14	0.52	0.65	-				
LOI	-0.15	1.08	-	-				
Total	99.49	100.53	101.52	99.99				
Mg# ^h	64.85	35.62	22.07	23.95				
La (µg/g)	3.1	13.3	20.6		0.06	0.09	0.11	0.16
Ce	9.6	42	61		0.06	0.10	0.11	0.19
Nd	8.3	40	58		0.11	0.18	0.20	0.30
Sm	3.05	-	18.2		0.17	0.27	0.30	0.42
Eu	1.09	3.30	4.82		0.21	0.29	0.35	0.45
Gd	4.25	-	23.5		0.22	0.32	0.35	0.49
Dy	5.25	16.2	27.0		0.22	0.33	0.37	0.50
Er	3.10	10.7	18.8		0.23	0.33	0.37	0.49
Yb	3.10	9.65	17.6		0.22	0.30	0.36	0.46

^a Parameters are defined in Table 1.

^b The z^E values are calculated from the bulk partition coefficients D^E (Table 1), considering two f values (1 and 0.5) and two cumulate modal compositions: 0.10 ol + 0.35 cpx + 0.55 plag for z_1^E (Rannou et al. 2006) and 0.043 ol + 0.447 cpx + 0.452 plag + 0.055 tmt + 0.003 ap for z_2^E (Perfit et al. 1983). Note that when $f=1$, z^E and D^E are equivalent.

^c Bas. = basalt; Fe-bas. = ferrobalt; And. = andesite; Dac. = dacite.

^d Location: NS = Northern Scarp; Galap. = Eastern Galapagos rift; Cleft = south Cleft segment.

^e WR = whole-rock analysis (ICP-AES); GL = glass analysis (EPMA).

^f References: 1. Cordier et al. (2007); 2. Fornari et al. (1983) and Perfit et al. (1983); 3. Stakes et al. (2006).

^g All Iron as Fe₂O₃^{tot}.

^h Mg# is calculated using a Fe₂O₃/FeO ratio of 0.2, 0.3 and 0.4 for basalt/ferrobalt, andesite, and dacite, respectively.

Table 3. Results of the modeling for the Cleft segment magma system in function of different values of C_{\max}^E , f and $Q_{\max}-Q_{\min}$ but similar values of C_{\min}^E (Table 2), r_c (0.4) and $[q_i]$ (0.004 km³/yr.10km).

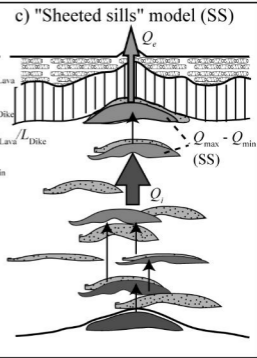
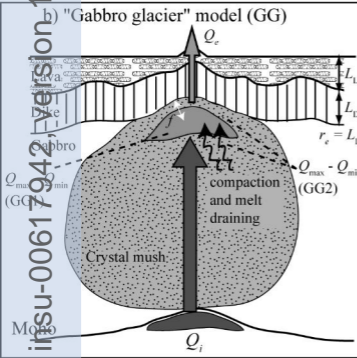
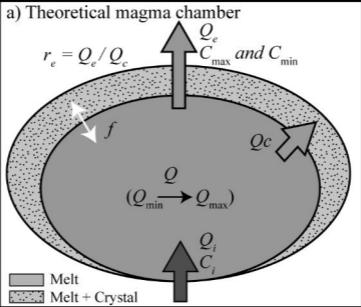
C_{\max}^E ¹	Fe-bas	Fe-bas	Andesite	Mg#=70
f	1	0.5	1	
Step 1: Composition of the modeled replenishment melt				
La (µg/g)	1.42	1.54	1.52	1.35
Ce	4.41	4.82	4.85	4.37
Nd	4.19	4.75	4.67	4.13
Sm			1.90	
Eu	0.62	0.72	0.70	0.69
Gd			2.80	
Dy	3.03	3.56	3.50	3.08
Er	1.82	2.13	2.05	1.90
Yb	1.78	2.09	2.02	1.83
β^{REE}	0.930-1.285	0.715-1.048	0.141-0.730	
β_{av}	1.137	0.899	0.467	
$\sigma(\beta_{\text{av}})$ ²	0.119	0.124	0.200	
Step 2: Crystallization rate (α), period (T), residence time (τ)				
GG ³ , $Q_{\max}-Q_{\min} = 0.45 \text{ km}^3/10\text{km}$				
α (yr ⁻¹)	0.0099	0.0107	0.0121	
T (yr)	561	654	1118	
τ (yr)	72	67	59	
GG ³ , $Q_{\max}-Q_{\min} = 0.63 \text{ km}^3/10\text{km}$				
α	0.0070	0.0076	0.0086	
T	785	916	1565	
τ	101	94	83	
SS ³ , $Q_{\max}-Q_{\min} = 0.9 \text{ km}^3/10\text{km}$				
α	0.0049	0.0053	0.0060	
T	1122	1308	2235	
τ	145	134	119	

¹ C_{\max} : composition of the most evolved lava considered in our calculations.

² $\sigma(\beta_{\text{av}})$: standard deviation of the β^E values deduced from the different REE.

³ GG: gabbro glacier model for the magma chamber, by ignoring or considering the partial draining of the crystal much lying beneath the melt lens; SS: sheeted sill model. See text for the estimation of the different volumes.

insu-00617942, version 1 - 31 Aug 2011



Cordier et al.
Figure 1

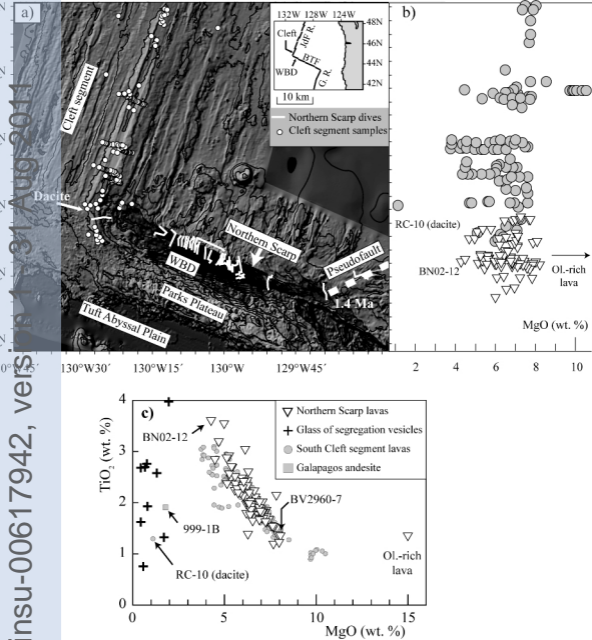


Figure 2
Cordier et al.

insu-00617942, vers 1.0 31 Aug 2011

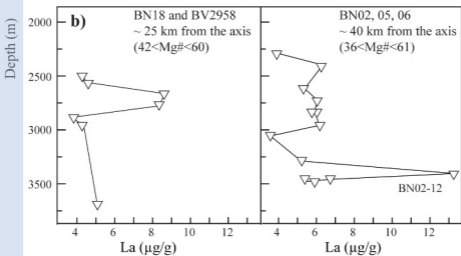
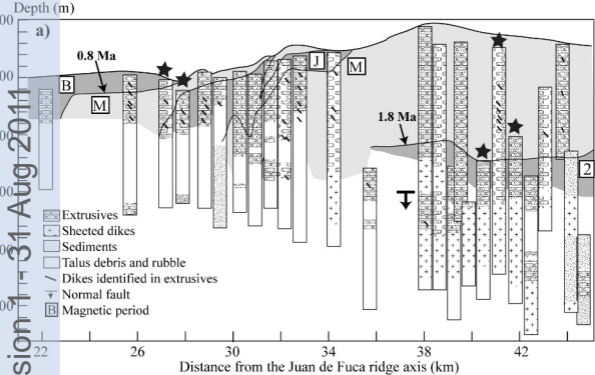


Figure 3
Cordier et al.

(a) Step 1: Geochemical approach

Required parameters:

$$\text{Eq. 1: } C^E(t) = C_i^E \frac{\frac{1}{z^E + r_e} + \left[\frac{\cos(\omega t - \arcsin \frac{\beta^E}{\sqrt{\beta^{E2} + (z^E + r_e)^2}})}{\sqrt{\beta^{E2} + (z^E + r_e)^2}} \right]}{\frac{1}{1 + r_e} + \left[\frac{\cos(\omega t - \arcsin \frac{\beta^E}{\sqrt{\beta^{E2} + (1 + r_e)^2}})}{\sqrt{\beta^{E2} + (1 + r_e)^2}} \right]}$$

$$\text{With Eq. 2: } z^E = \frac{D^E}{D^E(1-f) + f}$$

Results: β^E , β_{av} and C_i^E **(b) Step 2: Temporal approach**

Required parameters:

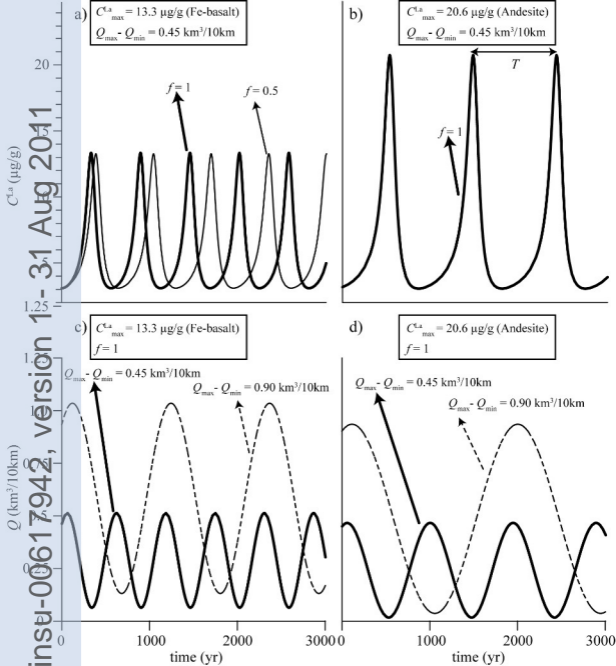
$$\text{Eq. 3: } \alpha = \frac{2[q_i]}{(Q_{\max} - Q_{\min}) \sqrt{\beta_{av}^2 + (1 + r_e)^2}}$$

$$\text{Eq. 4: } T = \frac{2\pi}{\alpha \beta_{av}}$$

$$\text{Eq. 5: } \tau = \frac{1}{\alpha(1 + r_e)}$$

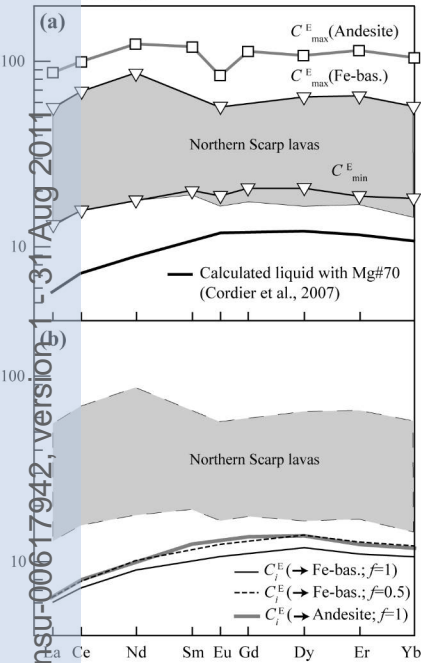
$$\text{Eq. 6: } Q(t) = \frac{[q_i]}{\alpha(1 + r_e)} + \frac{[q_i] \cos \left[\frac{2\pi}{T} t - \arcsin \left(\frac{\beta_{av}}{\sqrt{\beta_{av}^2 + (1 + r_e)^2}} \right) \right]}{\sqrt{\alpha^2(1 + r_e)^2 + \left[\frac{2\pi}{T} \right]^2}}$$

Results: α , T , τ , and Q Figure 4
Cordier et al.



Cordier et al.
 Figure 5

Rock/Chondrites



Cordier et al.
Figure 6